Research Square

Preprints are preliminary reports that have not undergone peer review.
They should not be considered conclusive, used to inform clinical practice,
or referenced by the media as validated information.

Monitoring of Antarctic Crustal Movement Based on Precise Point Positioning with Ambiguity Resolution Method

Chuanfeng Song
Liaoning Technical University
Xinning Pei
Liaoning Technical University
Huizhong Zhu
Liaoning Technical University
Qi Xu
47231055@stu.lntu.edu.cn

Liaoning Technical University
Yixi Wang
Liaoning Technical University
Xiudi Peng
Liaoning Technical University

Article

Keywords: GNSS PPP-AR Time series Velocity field Antarctic plate

Posted Date: November 10th, 2026

DOI: https://doi.org/10.21203/rs.3.rs-11347053/v1

License: This work is licensed under a Creative Commons Attribution 4.0 International License.
Read Full License

Additional Declarations: No competing interests reported.

Monitoring of Antarctic Crustal Movement Based on Precise Point Positioning with Ambiguity Resolution Method

Chuanfeng Song[1,2]·Xinning Pei[1]·Huizhong Zhu[1]·Qi Xu[1]·Yixi Wang[1]·Xiudi Peng[1]

✉ Qi Xu

47231055@stu.lntu.edu.cn

[1] School of Geomatics, Liaoning Technical University, Fuxin 123000, China

[2] Ordos Research Institute, Liaoning Technical University, Ordos 017004, China

Abstract High-precision monitoring of crustal motion in Antarctica is of great significance for investigating mass changes of the Antarctic Ice Sheet (AIS), environmental loading effects, and regional geodynamic processes. Precise Point Positioning (PPP) is an effective positioning technique in environments where reference stations are sparse, and PPP Ambiguity Resolution (AR) has clear advantages over float PPP. In this study, PPP and PPP-AR were respectively applied to process the combined Global Positioning System (GPS) and Galileo observations from eight Multi-Global Navigation Satellite System Experiment (MGEX) reference stations in Antarctica during 2020–2024, thereby obtaining long-term coordinate time series, and wavelet analysis, outlier detection, and time-series reconstruction were utilized to improve the quality of the coordinate time series. Based on the pre-processed coordinate time series, the horizontal velocity field was estimated utilizing least-squares linear fitting, and an Antarctic Plate motion model was constructed based on the rigid plate rotation assumption and Euler vector parameters. The results show that, compared with float PPP, PPP-AR can effectively reduce abnormal jumps and random fluctuations in the coordinate time series. Moreover, PPP-AR improves the average positioning accuracy in the North and East components by 7.80% and 24.65%, respectively. In addition, PPP-AR also improves the accuracy of horizontal velocity estimation, with improvements of 20.00% in the North component and 33.33% in the East component. The Euler vector model constructed utilizing six MGEX reference stations was validated with two

stations that were not involved in the modeling, and the velocity differences are generally at the millimeter level. The estimated Euler vector parameters are also in good agreement with those of the International Terrestrial Reference Frame 2020 Velocity Model (ITRF2020VEL). In conclusion, compared with float PPP, PPP-AR can effectively improve the quality of coordinate time series and the accuracy of horizontal velocity estimation for Antarctic stations, and can provide a methodological reference for Antarctic plate motion analysis and crustal deformation monitoring.

Keywords: GNSS PPP-AR Time series Velocity field Antarctic plate

Introduction

Antarctica is an important region for studies of the global climate system and geodynamics. Changes in the mass of the Antarctic Ice Sheet (AIS) can induce glacial isostatic adjustment (GIA) [1-3] and surface loading effects, thereby affecting regional crustal motion and plate motion studies [4-5]. The Global Navigation Satellite System (GNSS), characterized by all-weather operation, continuous observation, and high-precision positioning, has been widely utilized for crustal deformation, environmental loading, and velocity field monitoring [6-8]. With the continuous development of the observation and data infrastructure of the International GNSS Service (IGS) [9-10], long-term GNSS observations have gradually accumulated in Antarctica, providing an important data basis for obtaining high-precision coordinate time series and investigating regional crustal motion.

Precise Point Positioning (PPP) does not rely on nearby reference stations and can achieve high-precision single-station positioning utilizing precise satellite orbit and clock products [11-12], making it suitable for regions with sparse reference stations and limited infrastructure. However, conventional PPP generally estimates carrier-phase ambiguities as float parameters, and its positioning accuracy and convergence performance still have room for further improvement. To address this limitation, PPP Ambiguity Resolution (PPP-AR) has been widely investigated, and previous studies have demonstrated that re-covering the integer properties of carrier-phase ambiguities can effectively improve PPP positioning performance [13-14]. Nowadays, PPP-AR has

been extended to multi-frequency and multi-GNSS applications [15-16], further improving the applicability of PPP under complex observation conditions. Compared with conventional float PPP, PPP-AR has greater potential to improve coordinate estimation accuracy, enhance the stability of coordinate time series, and obtain high-quality long-term coordinate time series.

However, the GNSS coordinate time series obtained by PPP and PPP-AR method not only contain the long-term motion trends of reference stations, but may also be affected by outliers and missing data. Shen et al. [17] indicated that missing data are an important issue that should be considered in GNSS time-series processing. Ji et al. [18] processed the time series by performing outlier removal, offset correction, missing-data processing, and detrending before conducting data analysis. Ren et al. [19] emphasized that outliers and offsets in time series can affect data continuity as well as the estimation of linear and non-linear signals. Therefore, appropriate preprocessing of coordinate time series is an important prerequisite for crustal deformation analysis.

In studies of Antarctic crustal motion utilizing GNSS data, Bouin and Vigny [20] processed GPS observations through relative positioning method, obtained the horizontal velocities of Antarctic stations, and estimated the Antarctic Plate rotation parameters. Savchyn et al. [21] employed float PPP processing method to analyze the horizontal velocity field, strain characteristics, and rotation pole of continuous GNSS stations in Antarctica. Kellevezir et al. [22] also adopted a relative positioning approach to estimate station velocities on the Antarctic Plate and its surrounding plates, and further investigated the motion of the Antarctic Plate relative to adjacent plates. However, these studies mainly re-lied on GPS observations and did not fully exploit the advantages of combined multi-GNSS data. Moreover, systematic comparisons of coordinate time series derived from PPP and PPP-AR, as well as evaluations of their effects on Antarctic Plate motion modeling, remain relatively limited.

Therefore, this study focuses on evaluating the performance of multi-GNSS PPP and PPP-AR in Antarctic crustal movement monitoring. First, the fundamental theories in-volved in this study are introduced, including PPP and PPP-AR methods, wavelet

analysis methods, and plate motion model construction methods. Thereafter, the experimental data and processing strategies are described, followed by the corresponding experimental results. Finally, some conclusions are presented

Fundamental Theories

PPP Observation Model

For GNSS data processing, the ionosphere-free pseudorange and carrier-phase observation equations can be written as:

$$\begin{aligned} P_{r,IF}^{s} &= \rho_{r}^{s} + c(t_r - t^{s}) + T_{r}^{s} + e_{r,IF}^{s} \\ L_{r,IF}^{s} &= \rho_{r}^{s} + c(t_r - t^{s}) + T_{r}^{s} + \lambda_{IF} N_{r,IF}^{s} + \delta_{r,IF}^{s} \end{aligned} \tag{1}$$

where c is the speed of light, and T_r^s represents the tropospheric delay. The receiver and satellite clock offsets are denoted by t_r and t^s, respectively, while ρ_r^s represents the geometric range between the receiver and satellite antenna phase centers. λ_{IF} denotes the wavelength of the ionosphere-free combination, and $N_{r,IF}^s$ is the corresponding ambiguity parameter containing the receiver- and satellite-related hardware code and phase biases. The terms $e_{r,IF}^s$ and $\delta_{r,IF}^s$ account for observation noise and other unmodeled errors in the ionosphere-free pseudorange and carrier-phase observations, respectively. The sub-scripts and superscripts r and s identify the receiver and satellite, respectively.

In multi-GNSS PPP processing, receiver hardware code biases associated with different signal frequencies can be absorbed into the receiver clock parameters. Instead of estimating an independent receiver clock parameter for each frequency, an Inter-System Bias (ISB) can be introduced to describe the bias between a non-reference satellite system and the selected reference system [23]. With GPS adopted as the reference system and frequency division multiple access systems excluded, the multi-GNSS PPP observation model can be written as:

$$
\begin{aligned}
P_{r,IF}^{g} &= \rho_r^g + c\cdot\left(t_r^G - t^g\right) + T_r^g + e_{r,IF}^g \\
L_{r,IF}^{g} &= \rho_r^g + c\cdot\left(t_r^G - t^g\right) + \lambda_{IF}^g \cdot N_{r,IF}^g + T_r^g + \delta_{r,IF}^g \\
P_{r,IF}^{a} &= \rho_r^a + c\cdot\left(t_r^G + t_r^{AG} - t^a\right) + T_r^a + e_{r,IF}^a \\
L_{r,IF}^{a} &= \rho_r^a + c\cdot\left(t_r^G + t_r^{AG} - t^a\right) + \lambda_{IF}^a \cdot N_{r,IF}^a + T_r^a + \delta_{r,IF}^a
\end{aligned}
\tag{2}
$$

where t_r^{AG} represents the ISB parameter; t_r^G denotes the receiver clock offset associated with the GPS system; A and refer to the non-reference satellite system and a satellite belonging to that system, respectively; G and g represent the GPS system and a GPS satellite, respectively.

The above observation equations are linearized, and error equations are constructed by combining the actual observation values with the approximate values of the unknown parameters. Then, the error equations are solved based on the least-squares principle, thereby achieving float PPP solutions.

PPP Ambiguity Resolution Method

This paper achieves PPP ambiguity resolution based on the uncalibrated phase delay (UPD) method [13-14]. The wide-lane (WL) between-satellite single-difference ambiguities are first derived from the Hatch Melbourne-Wübbena (HMW) combination [24-26]. To suppress observation noise, the HMW combinations are averaged over multiple epochs. The resulting WL ambiguities are subsequently corrected with the WL UPD products, after which their integer properties are recovered by rounding:

$$
N_{r,WL}^{ss_0} = \hat{N}_{r,WL}^{ss_0} - UPD_{WL}^{ss_0} \tag{3}
$$

where $UPD_{WL}^{ss_0}$ represents the corresponding wide-lane fractional cycle bias; $N_{r,WL}^{ss_0}$ de-notes the fixed between-satellite single-difference wide-lane ambiguity; and $\hat{N}_{r,WL}^{ss_0}$ refers to the wide-lane single-difference float ambiguity formed at receiver r between satellite s and the reference satellite s_0.

After the WL ambiguities are resolved, the narrow-lane (NL) float ambiguities are de-rived from the ionosphere-free ambiguities obtained from the PPP float solution.

The Least-squares Ambiguity Decorrelation Adjustment (LAMBDA) method [27] is subsequently utilized to decorrelate the NL ambiguities, and reliable NL integer ambiguities are determined through a ratio test together with additional validation criteria.

Once both the WL and NL ambiguities have been successfully resolved, the integer nature of the ionosphere-free ambiguity can be restored, as given by:

$$N_{r,IF}^{ss_0} = \left(\frac{cf_2}{f_1^2 - f_2^2} N_{r,WL}^{ss_0} + \frac{c}{f_1 + f_2} \left(N_{r,NL}^{ss_0} - UPD_{NL}^{ss_0} \right) \right) / \lambda_{IF} \tag{4}$$

where f_1 and f_2 represent the carrier frequencies, $N_{r,IF}^{ss_0}$ denotes the fixed ionosphere-free combination ambiguity. Once the integer nature of the ionosphere-free ambiguity has been restored, it is incorporated into the normal equation in the form of a virtual observation. The corresponding weight is determined from the ambiguity precision together with the UPD error level. The constrained ambiguity information is then combined with the PPP float solution model to derive the ambiguity-fixed PPP solution.

Wavelet Analysis Method

This paper utilized wavelet analysis to detect anomalous data. Wavelet analysis serves as an effective tool for time-series analysis [18], capable of extracting localized features of signals in both the time and frequency domains. Characterized by multi-scale resolution, it enables a hierarchical decomposition of data ranging from overall profiles to local details. The fundamental principle involves adjusting the scale parameter and translation factor to capture the distributional characteristics of the signal waveform across various frequency components, thereby simultaneously characterizing global trends and local transients. A primary advantage of wavelet analysis is its ability to not only identify the frequency components of a signal but also precisely locate the temporal distribution of these components along the time axis.

A wavelet function is a function with finite energy and a zero mean, expressed as:

$\psi(x) \in L^2(R)$, A family of wavelet functions $\{\psi_{a,b}\}$ can be generated by scaling and translating a given wavelet function.

$$\psi_{a,b}(x) = \frac{1}{\sqrt{a}}\psi(\frac{x-b}{a}) \tag{5}$$

$$W_{f(a,b)} = \langle f, \psi_{a,b} \rangle = \int_{-\infty}^{+\infty} \psi_{a,b}^*(x)dx = \int_{-\infty}^{+\infty} f(x)\frac{1}{\sqrt{a}}\psi^*(\frac{x-b}{a})dx \tag{6}$$

The wavelet transform is defined as the decomposition of a finite-energy signal utilizing wavelet functions as basic functions. Here, "< >" denotes the inner product, and "*" represents the complex conjugate. In the above wavelet transform, the wavelet coefficient $W_f(a,b)$ reflects the degree of similarity between the signal and the wavelet function $\psi_{a,b}(x)$. The parameter a represents the scale factor, while the parameter b denotes the translation parameter. The pair (a, b) thus defines a two-dimensional space of scale and local position.

With respect to an orthonormal basis $\{\psi_{k,n}\}$ in the space $L^2(\Re)$, the signal X_t can be decomposed into a wavelet series:

$$\begin{aligned} X(t) &= \sum_{k,l=-\infty}^{+\infty} c_{k,l}\varphi_{k,l}(t) \\ \varphi_{k,l}(t) &= 2^{-k/2}\varphi(2^{-k}t - l), k, l \in Z \end{aligned} \tag{7}$$

In the formula, $\varphi_{k,l}$ denotes the dyadic wavelet, which provides multi-scale resolution for signal analysis. Furthermore, the dyadic wavelet preserves the translation invariance of the signal in the time domain, providing an advantage for time-domain signal analysis. Let $\psi(x) \in L^2(R)$ represent the wavelet in R and $\bar{\psi}(x) \in L^2(\Re)$ denote its dual, expressed as:

$$\begin{aligned} \psi_{k,l}(x) &:= 2^{-k/2}\psi(2^{-k}x - l) \\ \bar{\psi}_{k,l}(x) &:= 2^{-k/2}\bar{\psi}(2^{-k}x - l) \end{aligned} \tag{8}$$

Each function $f \in L^2(\Re)$ is characterized by the following representation:

$$f(x)=\int_{-\infty}^{+\infty}\left\langle f,\psi_{k,l}\right\rangle\overline{\psi}_{k,l}(x)=\int_{-\infty}^{+\infty}\left\langle f,\overline{\psi}_{k,l}\right\rangle\psi_{k,l}(x) \tag{9}$$

Since $\psi(x)$ is an R-wavelet and $\{\psi_{k,l}\}$ is the Riesz basis of $L^2(\Re)$ generated by it, for each fixed k, let $W_k := clos_{L^2(\Re)}$ be defined such that W_k is the closure of the linear span of $\{\psi_{k,l} : n \in Z\}$. Consequently, $L^2(\Re)$ can be decomposed as:

$$L^2(\Re)=\cdots\oplus W_1\oplus W_0\oplus W_{-1}\cdots \tag{10}$$

In this case, $f \in L^2(\Re)$ possesses a unique solution:

$$f=\cdots+g_1+g_0+g_1+\cdots \tag{11}$$

Wavelet analysis is characterized by its multi-resolution properties. Wavelet multi-resolution analysis (MRA) facilitates the decomposition of the annual and semi-annual terms within the vertical coordinate time series of reference stations, effectively functioning as both an annual and a semi-annual mathematical filter. The schematic of multi-resolution analysis for signals is illustrated in Figure 1:

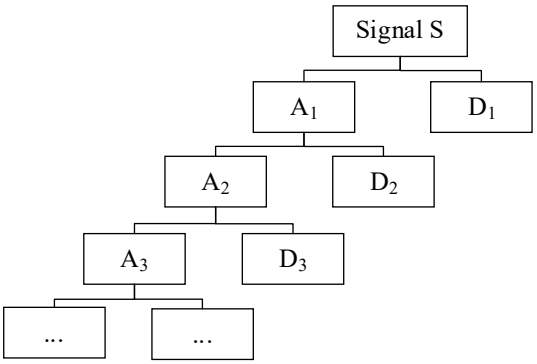


Fig. 1 Structure of Wavelet Analysis.

In Figure 1, A represents the low-frequency component of the signal, while D denotes the high-frequency component. Following the procedure illustrated in the figure, the coordinate time series is decomposed utilizing Symlets wavelets, followed by single-branch reconstruction at each decomposition level. The wavelet decomposition can be expressed as follows:

$$A_{k+1}=HA_K, K=1,2,\cdots,N \tag{12}$$

$$D_{k+1} = GD_K, K = 1,2,\cdots,N \tag{13}$$

The expression for the wavelet reconstruction is as follows:

$$A_{k+1} = H^* A_{k+1} + G^* D_{k+1}, K = N,\cdots,2,1 \tag{14}$$

where H and G denote the wavelet low-pass and high-pass filters, respectively; H^* and G^* represent their corresponding dual operators, which can generally be interpreted as the conjugate transpose matrices of H and G.

Plate Motion Model Construction Method

Assume that the preprocessed coordinate time series contains n valid epochs. For the i^{th} epoch, denoted by t_i (in years), the univariate linear observation equation for the coordinate displacement observation $y(t_i)$ can be formulated as:

$$y(t_i) = v \cdot t_i + y_0 + \varepsilon_i \tag{15}$$

where $y(t_i)$ denotes the coordinate observation at epoch t_i, v represents the station velocity to be estimated, y_0 is the initial coordinate offset with respect to the reference epoch, and ε_i denotes the observation residual corresponding to that epoch.

The observation equation described above can be rewritten in matrix form as:

$$L = \begin{bmatrix} y(t_1) \\ y(t_2) \\ \vdots \\ y(t_n) \end{bmatrix}, \quad B = \begin{bmatrix} t_1 & 1 \\ t_2 & 1 \\ \vdots & \vdots \\ t_n & 1 \end{bmatrix}, \quad X = \begin{bmatrix} v \\ y_0 \end{bmatrix} \tag{16}$$

According to the least-squares criterion, the normal-equation solution for the velocity parameter vector X is given by:

$$\hat{X} = (B^T B)^{-1} B^T L \tag{17}$$

By solving this matrix equation, the first element of the parameter vector $\hat{X}$ is obtained as the estimated station velocity $\hat{v}$.

In crustal kinematics, plate tectonic movement is conventionally modeled as the rotation of a rigid body on a spherical surface [28]. This motion can be quantitatively de-scribed by the Euler vector Ω.

Its representation encompasses either spherical coordinate components (angular velocity ω, Euler pole latitude ϕ, and Euler pole longitude Λ) or Cartesian coordinate components (Ω_x, Ω_y, and Ω_z). Under the assumption of rigid rotation of the Antarctic plate, the relationship between the eastward and northward velocity components of each station and the Cartesian components of the Euler vector can be expressed as follows:

$$\begin{bmatrix} v_e \\ v_n \end{bmatrix} = r \begin{bmatrix} -\cos L \sin B & -\sin L \sin B & \cos B \\ \sin L & -\cos L & 0 \end{bmatrix} \begin{bmatrix} \Omega_x \\ \Omega_y \\ \Omega_z \end{bmatrix} \tag{18}$$

In the equation, v_e and v_n represent the East (E) and North (N) horizontal velocity components of the reference station, respectively; r denotes the radius, while L and B indicate the longitude and latitude of the station. Based on this equation, the three com-ponents of the Euler vector in the Cartesian coordinate system can be determined. Subsequently, these Cartesian components are transformed into spherical coordinates to derive the spherical coordinate components of the Euler vector, as expressed in Equation (19).

$$\left.\begin{aligned} \omega &= \sqrt{\Omega_x^2 + \Omega_y^2 + \Omega_x^2} \\ \phi &= \arcsin(\Omega_z / \omega) \\ \Lambda &= \arcsin(\Omega_y / \Omega_x) \end{aligned}\right\} \tag{19}$$

where the value range of ϕ is $(-\frac{\pi}{2}, \frac{\pi}{2})$, and that of Λ is $(-\pi, \pi)$. If $\Omega_y > 0$ and $\Omega_x < 0$,then $\Lambda = \arcsin(\Omega_y / \Omega_x) + \frac{\pi}{2}$;if $\Omega_y < 0$ and $\Omega_x < 0$,then $\Lambda = \arcsin(\Omega_y / \Omega_x) - \frac{\pi}{2}$.

Experimental Data and Strategies

This study selects eight continuously operating GNSS reference stations covering the Antarctic continent and its surrounding islands, including CAS1, DAVI, MAW1, MCM4, OHI3, PALM, SYOG, and ARHT. The station distribution is shown in Figure 2, and the observation period spans from January 1, 2020 to December 31, 2024.

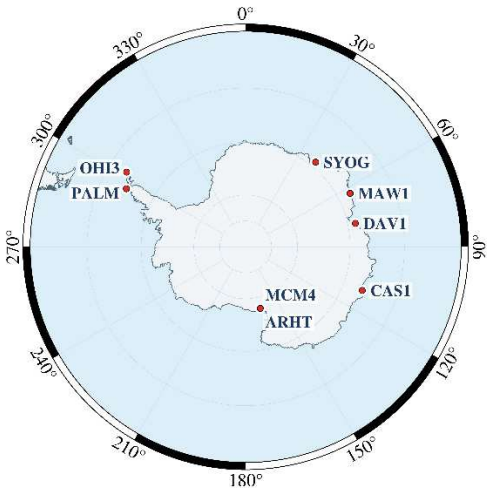


Fig 2. Geographical Distribution of Antarctic GNSS Stations

To analyze the variation characteristics of the coordinate time series of GNSS reference stations in Antarctica and to compare the performance of PPP and PPP-AR, the processing workflow shown in Figure 3 is adopted. The overall procedure includes GNSS observation collection, PPP and PPP-AR processing, coordinate time-series generation, missing-data interpolation, outlier removal, and time-series reconstruction. Based on the preprocessed coordinate time series, the velocity field was estimated and the Euler vector model was constructed, followed by a comparative analysis of the PPP and PPP-AR results.

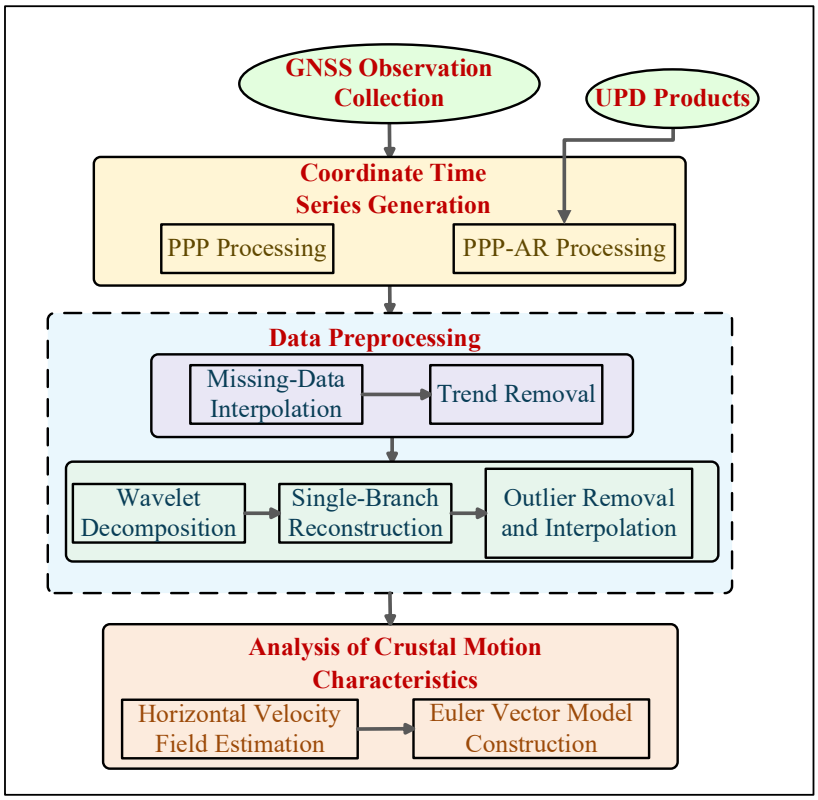


Fig 3. Technical Roadmap

To ensure the stability and reliability of the processing results, combined GPS and Galileo observations were processed in this study. During data processing, the Phase Center Offset (PCO) and Phase Center Variation (PCV) were corrected according to the IGS conventions, while the effects of solid Earth tides, ocean tides, and pole tides were corrected according to the International Earth Rotation and Reference Systems Service (IERS) conventions [29]. Phase wind-up, Earth rotation, and relativistic effects were also corrected during PPP processing to reduce the influence of systematic errors on the coordinate solutions. The main observation models, error corrections, and parameter settings adopted in this study are summarized in Table 1.

Table 1 Data Processing Strategies

Parameter	Model
Observations	Ionosphere-free combination (pseudorange + carrier phase)
Frequencies	GPS: L1, L2; Galileo: E1, E5a
Sampling interval	30 s
Processing duration	24 h
Elevation cutoff angle	7°
UPD	WHU multi-GNSS UPD products
Satellite orbit	WHU multi-GNSS precise orbit products
Satellite clock offset	WHU multi-GNSS precise clock offset products
Ionospheric delay	Eliminated by the ionosphere-free combination
Tropospheric delay	Saastamoinen model + Zenith Total Delay (ZTD) estimation
Receiver clock offset	Estimated epoch by epoch
Station coordinates	Estimated as constants
ISB parameters	Estimated as constants
Ambiguities	Estimated as arc-wise constants

Experimental Results and Analysis

Comparison of PPP and PPP-AR Positioning Accuracy

To evaluate the positioning accuracy of PPP and PPP-AR, the IGS weekly solutions were utilized as the reference coordinates, and the positioning accuracy of the Antarctic stations in the N, E, and Up (U) components were assessed. The results are shown in Table 2.

Table 2 Positioning Accuracy of PPP and PPP-AR Relative to IGS Weekly Solution

Station	PPP_N (mm)	PPP_E (mm)	PPP_U (mm)	PPP-AR_N (mm)	PPP-AR_E (mm)	PPP-AR_U (mm)
ARHT	3.51	4.10	10.89	2.71	4.08	9.80
CAS1	3.91	4.86	12.22	3.47	3.70	10.88
DAV1	3.66	5.17	8.57	4.15	2.59	8.69
MAW1	4.02	3.55	5.81	3.43	2.06	4.52
MCM4	3.22	3.84	7.44	2.43	2.81	7.07
OHI3	6.04	4.74	10.04	5.89	4.34	7.32
PALM	4.37	4.17	7.20	4.95	3.34	6.39
SYOG	4.10	3.61	7.11	3.21	2.74	6.42
Average	4.10	4.26	8.66	3.78	3.21	7.64

As shown in Table 2, PPP-AR improves the positioning accuracy of PPP through ambiguity resolution. The improvement is particularly evident in the E component, where the average positioning error decreases from 4.26 mm to 3.21 mm, corresponding to an improvement of approximately 24.65%. In the U component, the average positioning error decreases from 8.66 mm to 7.64 mm, corresponding to an improvement of approximately 11.78%. In the N component, the average positioning error decreases from 4.10 mm to 3.78 mm, corresponding to an improvement of approximately 7.80%. These results indicate that ambiguity resolution can effectively improve the positioning accuracy and provide a reliable data source for subsequent analysis of coordinate time series.

Raw Horizontal Coordinate Time Series n

Taking the CAS1 station as an example, Figures 4–5 show the raw horizontal coordinate time series obtained utilizing float PPP and PPP-AR, respectively.

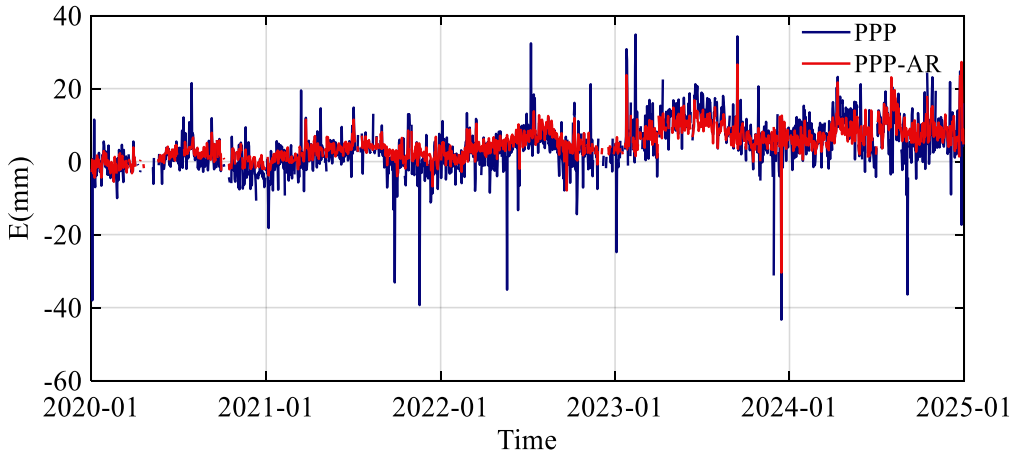


Fig 4. Raw East-Component Time Series of CAS1 in PPP and PPP-AR Modes

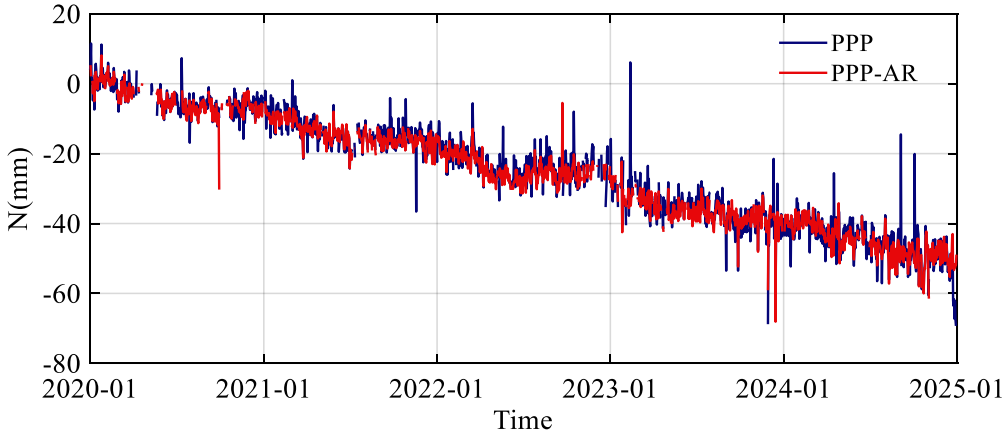


Fig 5. Raw North-Component Time Series of CAS1 in PPP and PPP-AR Modes

As shown in Figures 4–5, the horizontal coordinate time series obtained from both float PPP and PPP-AR processing modes contain local jumps and missing data, which may be related to the harsh environmental conditions in Antarctica, instrument failures, and other factors. After ambiguity resolution in PPP-AR, the horizontal coordinate time series become smoother, abnormal fluctuations are reduced, and the overall quality is markedly improved.

Time-Series Outlier Detection and Quality Control

In long-term horizontal coordinate time series, outliers can affect velocity field estimation. Therefore, orthogonal polynomial interpolation [30] was first applied to the horizontal coordinate time series of each station. When relatively long periods of consecutive data are missing, this interpolation method can effectively preserve the original temporal variation trend. The linear trend was then removed from the horizontal coordinate time series, and the series was decomposed utilizing Symlets wavelets. After individual reconstruction of the wavelet coefficients and removal of the effects of the high- and low-frequency components, outliers with residuals greater than three times the standard deviation were removed from the residual series. The removed high- and low-frequency components were subsequently restored, and cubic spline interpolation was applied to fill the missing data, thereby obtaining a more continuous and smooth coordinate time series. When only a small number of consecutive data points are missing, cubic spline interpolation provides satisfactory results.

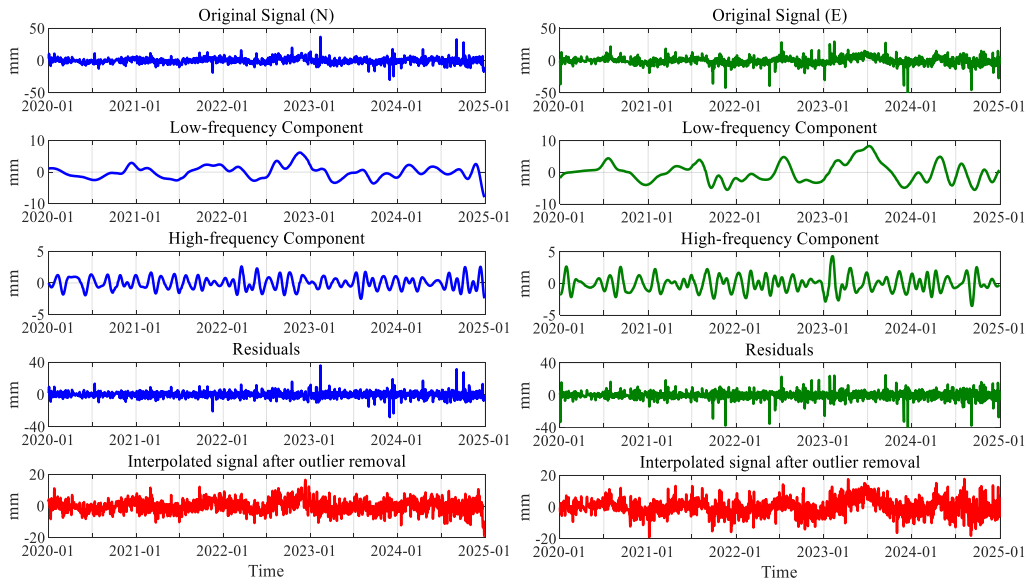


Fig 6. Results of Outlier Detection and Quality Control for CAS1 in PPP Mode

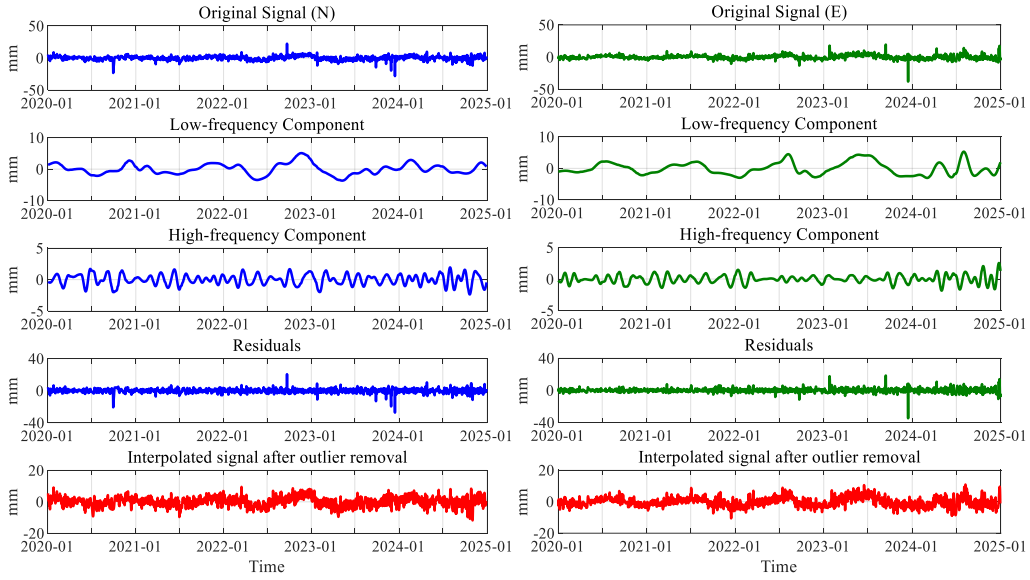


Fig 7. Results of Outlier Detection and Quality Control for CAS1 in PPP-AR Mode

Figures 6 and 7 show the results of outlier detection and quality control for the CAS1 station under PPP and PPP-AR, respectively. After outlier removal, the quality of the coordinate time series obtained from both processing modes is effectively improved, with a significant reduction in abnormal data points. However, the PPP-AR coordinate time series exhibits smaller fluctuations and higher overall quality.

Comparison of the residual series shows that the horizontal coordinate time series obtained from PPP-AR is smoother than that obtained from PPP, indicating that ambiguity resolution can effectively improve the stability of the coordinate time series and provide a reliable data basis for subsequent coordinate time-series analysis.

Crustal Motion Monitoring

Based on the N- and E-direction coordinate time series obtained from PPP and PPP-AR, least-squares linear fitting was applied to estimate the northward and eastward velocities of each station, respectively, and the standard errors of the fitted velocities were utilized to evaluate the accuracy of velocity estimation.

Figures 8 and 9 show the linear fitting results of the N- and E-direction coordinate time series for representative stations CAS1 and MCM4, and Table 3 lists the horizontal velocities and their standard errors for the eight reference stations under PPP and PPP-AR modes. Based on the N- and E-direction velocities of each station, the horizontal velocity field of the Antarctic reference stations was plotted, as shown in Figure 10.

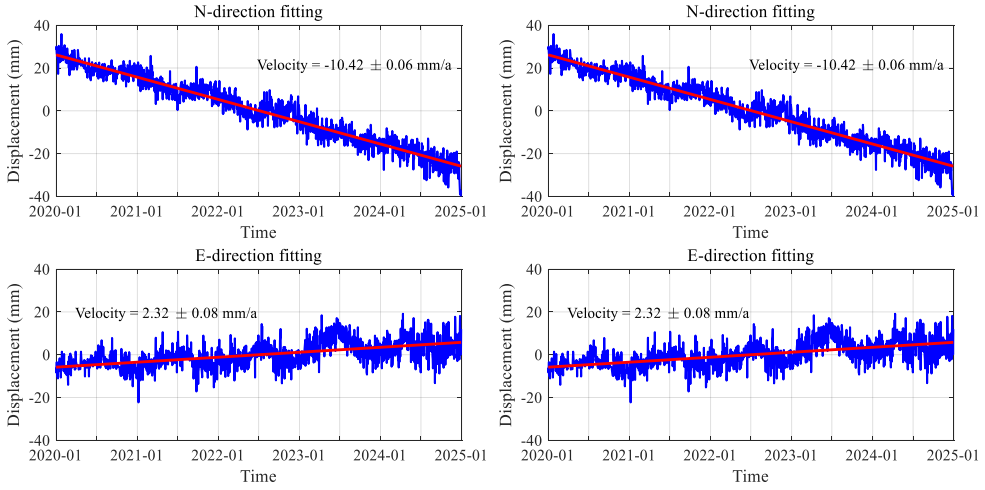


Fig 8. Coordinate fitting of CAS1 station under PPP and PPP-AR solutions

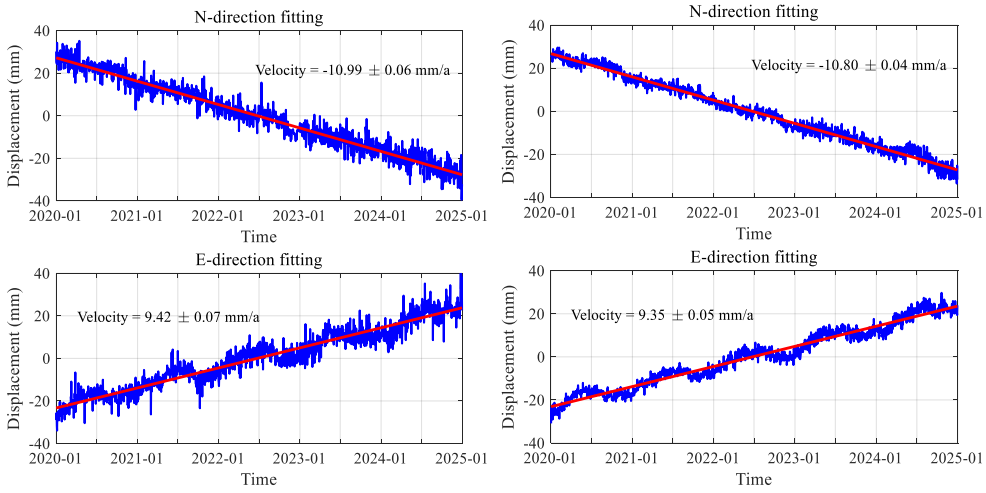


Fig 9. Coordinate fitting of MCM4 station under PPP and PPP-AR solutions

Table 3 Comparison of horizontal velocity fitting results between PPP and PPP-AR for Antarctic stations

Station	Model	vN (mm/a)	σN (mm/a)	vE (mm/a)	σE (mm/a)
CAS1	PPP	-10.42	0.06	2.32	0.08
	PPP-AR	-10.33	0.05	1.94	0.05
ARHT	PPP	-10.75	0.05	9.09	0.06
	PPP-AR	-10.61	0.04	9.09	0.05
DAV1	PPP	-6.27	0.08	-2.27	0.08
	PPP-AR	-5.91	0.06	-2.16	0.04
MAW1	PPP	-2.83	0.08	-3.29	0.07
	PPP-AR	-2.79	0.07	-3.32	0.05
MCM4	PPP	-10.99	0.06	9.42	0.07
	PPP-AR	-10.80	0.04	9.35	0.05
OHI3	PPP	10.78	0.08	13.30	0.09
	PPP-AR	10.67	0.07	13.15	0.06
PALM	PPP	8.93	0.07	13.91	0.08
	PPP-AR	9.07	0.06	13.82	0.06
SYOG	PPP	1.37	0.07	-3.70	0.07
	PPP-AR	1.43	0.05	-3.47	0.04
Mean	PPP	-	0.069		0.075
	PPP-AR	-	0.055		0.050

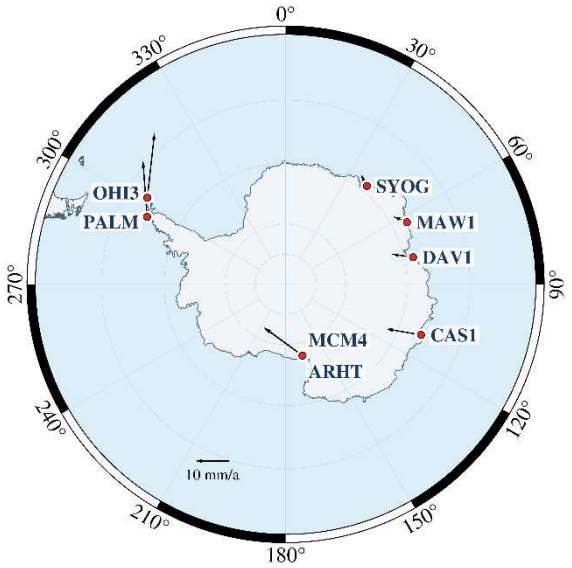


Fig 10. Horizontal velocity field of Antarctic reference stations

As shown in Figures 8 and 9 and Table 3, the standard errors of the velocity estimates obtained from PPP-AR are smaller than those obtained from float PPP because the ambiguity parameters were fixed in PPP-AR. For example, at the CAS1 station, the standard errors of the E- and N-direction velocities under PPP are 0.08 mm/a and 0.06 mm/a, respectively, whereas both are reduced to 0.05 mm/a under PPP-AR. As shown in Table 3, the average standard errors of the N- and E-direction velocities under PPP-AR are 0.055 mm/a and 0.050 mm/a, respectively, and the Root Mean Square (RMS) of the horizontal velocity vector is 0.075 mm/a. The corresponding values under PPP are 0.069 mm/a, 0.075 mm/a, and 0.103 mm/a, respectively. Compared with PPP, the accuracy of the N- and E-direction velocity estimates under PPP-AR is improved by approximately 20.00% and 33.33%, respectively. These results indicate that PPP-AR can effectively improve the accuracy of the Antarctic horizontal velocity field, with a more pronounced improvement in the E direction.

Considering the geographical distribution of the reference stations, the horizontal velocity components of six reference stations were utilized as observations to construct the model, while MAW1 and OHI3 were selected as external validation stations. According to Eq. (18), the Cartesian components of the Euler vector were estimated

under the least-squares criterion and then transformed into spherical coordinates to construct the Antarctic Plate motion model. To evaluate the accuracy and reliability of the model, the horizontal velocities of all eight reference stations were calculated from the model and compared with the fitted velocities derived from the coordinate time series. As shown in Tables 4 and 5, the model accuracy was evaluated based on the modeling stations and validation stations.

Table 4 Fitness Analysis of the Euler Vector Model Based on the PPP Solution

Station Name	Station Type	Fitting vN (mm/a)	Model vN (mm/a)	ΔvN (mm/a)	Fitting vE (mm/a)	Model vE (mm/a)	ΔvE (mm/a)
CAS1	Modeling Station	-10.42	-10.15	0.27	2.32	2.73	0.41
ARHT	Modeling Station	-10.75	-10.63	0.12	9.09	9.28	0.19
DAV1	Modeling Station	-6.27	-5.33	0.94	-2.27	-2.32	-0.05
MAW1	Validation Station	-2.83	-2.41	0.42	-3.29	-2.88	0.41
MCM4	Modeling Station	-10.99	-10.63	0.36	9.42	9.28	-0.14
OHI3	Validation Station	10.78	11.15	0.37	13.30	12.59	-0.71
PALM	Modeling Station	8.93	10.67	1.74	13.91	13.22	-0.69
SYOG	Modeling Station	1.37	2.35	0.98	-3.70	-3.46	0.24

Table 5 Fitness Analysis of the Euler Vector Model Based on the PPP-AR Solution

Station Name	Station Type	Fitting vN (mm/a)	Model vN (mm/a)	ΔvN (mm/a)	Fitting vE (mm/a)	Model vE (mm/a)	ΔvE (mm/a)
CAS1	Modeling Station	-10.33	-10.08	0.25	1.94	2.68	0.74
ARHT	Modeling Station	-10.61	-10.57	0.04	9.09	9.19	0.10
DAV1	Modeling Station	-5.91	-5.28	0.63	-2.16	-2.33	-0.17
MAW1	Validation Station	-2.79	-2.37	0.42	-3.32	-2.88	0.44
MCM4	Modeling Station	-10.80	-10.57	0.23	9.35	9.19	-0.16
OHI3	Validation Station	10.67	11.07	0.40	13.15	12.51	-0.64
PALM	Modeling Station	9.07	10.60	1.53	13.82	13.14	-0.68
SYOG	Modeling Station	1.43	2.36	0.93	-3.47	-3.45	0.02

Overall, under both PPP and PPP-AR, the differences between the velocities calculated from the Euler vector model and the fitted station velocities are mainly at the millimeter level. No obvious systematic differences are observed between the modeling stations and the validation stations, indicating that the constructed Euler vector models can effectively describe the overall horizontal motion characteristics of the Antarctic Plate. Compared with PPP, the velocity differences at most modeling stations are reduced under PPP-AR. For example, the N-direction difference at DAV1 decreases from 0.94 mm/a to 0.63 mm/a, that at PALM decreases from 1.74 mm/a to 1.53 mm/a, and that at MCM4 decreases from 0.36 mm/a to 0.23 mm/a. ARHT shows good agreement with the model, with N- and E-direction differences of only 0.04 mm/a and 0.10 mm/a, respectively, under PPP-AR. The smallest E-direction difference is observed at SYOG, with a value of only 0.02 mm/a. For the validation stations, under PPP, the N- and E-direction differences at MAW1 are 0.42 mm/a and 0.41 mm/a, respectively, while those at OHI3 are 0.37 mm/a and 0.71 mm/a. Under PPP-AR, the

corresponding differences at MAW1 are 0.42 mm/a and 0.44 mm/a, while those at OHI3 are 0.40 mm/a and 0.64 mm/a. Overall, the fitted station velocities show good agreement with the velocities calculated from the Euler vector models, indicat-ing that the Euler vector models established from the PPP and PPP-AR velocity fields can reliably reflect the overall horizontal motion of the Antarctic Plate.

To further validate the model developed in this study, the obtained Euler vector parameters were compared with those of the ITRF2020VEL [31]. The corresponding result is shown in Table 6.

Table 6 Comparison of Euler vector parameters between PPP, PPP-AR and ITRF2020VEL models

Model	$\omega/\left((^\circ)/\mathrm{Ma}\right)$	$\phi/(^\circ N)$	$\Lambda/(^\circ E)$
PPP-AR model	0.210	59.8	-128.8
PPP model	0.212	59.9	-128.9
ITRF2020VEL	0.220	58.6	-130.7

As shown in Table 6, the angular velocities of the PPP and PPP-AR models differ from that of ITRF2020VEL by 0.008 °/Ma and 0.010 °/Ma , respectively. The differences in Euler pole latitude are 1.3° and 1.2°, while those in Euler pole longitude are 1.8° and 1.9°, respectively. However, the PPP and PPP-AR models show little difference. Overall, the Euler vector parameters obtained from the PPP and PPP-AR models show good agreement with the ITRF2020VEL results, indicating that the Antarctic Plate motion models constructed in this study are reliable.

Conclusions

This study systematically compared the positioning performance of PPP and PPP-AR under the complex Antarctic observation environment utilizing five years of continuous multi-GNSS observations from eight MGEX reference stations. Through coordinate time-series processing, horizontal velocity estimation, and Euler vector model construction, the following main conclusions are obtained:

(1) By fixing integer ambiguities, PPP-AR effectively reduces coordinate jumps and random fluctuations in the PPP results, resulting in more continuous and stable

station coordinate time series.

(2) In the horizontal motion analysis, the standard errors of the velocity estimates obtained from PPP-AR are smaller than those obtained from PPP, providing a more reliable horizontal velocity field.

(3) Based on the high-precision horizontal velocity field and the rigid plate rotation assumption, an Antarctic Plate motion model was constructed utilizing six reference stations, with the remaining two stations utilized for external validation. The residuals at both the modeling and validation stations are at millimeter level. In addition, the estimated Euler vector parameters are in good agreement with those of the ITRF2020VEL plate motion model, confirming the rigid rotation characteristics of the Antarctic Plate and the reliability of the proposed modeling approach.

In summary, multi-GNSS PPP-AR demonstrates better positioning performance than conventional PPP for high-precision crustal deformation monitoring under the harsh Antarctic environment. Combined with wavelet analysis, PPP-AR can provide high-precision station coordinates and a reliable horizontal velocity field. Therefore, PPP-AR is feasible for Antarctic crustal movement monitoring and can provide reliable methodological support for analyzing Antarctic Plate deformation.

Acknowledgments

We acknowledge the IGS for providing the MGEX observation data, precise ephemeris, precise clocks, and other related products.

Data Availability

The MGEX observation data and precise products utilized by this study are available from the website: http://www.igs.gnsswhu.cn/. The other datasets are available from the corresponding author on reasonable request.

Author contribution

C.S. and X.P. processed the data and wrote the main manuscript text. H.Z. prepared the figures. Q.X., Y.W., and X.P. provided the methodological framework. All authors reviewed the manuscript.

Funding

This study is partially supported by the National Natural Science Foundation of China (42664004), and the Natural Science Foundation of Liaoning Province, China (2025-BS-0398).

Compliance with Ethical Standards

This article does not contain any studies with animals performed by any of the authors. Informed consent was obtained from all individual participants included in the study.

Consent for publication: All authors approved the final manuscript and the submission to this journal.

Competing Interests: The authors declare no conflict of interest.

References

1. Lecavalier B S, Tarasov L. A history-matching analysis of the Antarctic Ice Sheet since the last interglacial–Part 2: Glacial isostatic adjustment[J]. The Cryosphere, 2025, 19(12): 6673-6689.
2. Whitehouse P L, Gomez N, King M A, et al. Solid Earth change and the evolution of the Antarctic Ice Sheet[J]. Nature communications, 2019, 10(1): 503.
3. Barletta V R, Bevis M, Smith B E, et al. Observed rapid bedrock uplift in

Amundsen Sea Embayment promotes ice-sheet stability[J]. Science, 2018, 360(6395): 1335-1339.

4. Vardić K, Clarke P J, Whitehouse P L. A GNSS velocity field for crustal deformation studies: The influence of glacial isostatic adjustment on plate motion models[J]. Geophysical Journal International, 2022, 231(1): 426-458.
5. Willen M O, Wouters B, Broerse T, et al. Satellite data reveal details of glacial isostatic adjustment in the Amundsen Sea Embayment, West Antarctica[J]. EGUsphere, 2024, 2024: 1-24.
6. Tunini L, Magrin A, Rossi G, et al. Global Navigation Satellite System (GNSS) time series and velocities about a slowly convergent margin processed on high-performance computing (HPC) clusters: products and robustness evaluation[J]. Earth System Science Data, 2024, 16(2): 1083-1106.
7. Lv H, He X, Hu S. Investigating surface loading effect on seasonal crustal deformation observed by GNSS in Hong Kong[J]. Scientific Reports, 2025, 15(1): 2742.
8. Li X, Ge M, Dai X, et al. Accuracy and reliability of multi-GNSS real-time precise positioning: GPS, GLONASS, BeiDou, and Galileo[J]. Journal of geodesy, 2015, 89(6): 607-635.
9. Noll C, Bock Y, Habrich H, et al. Development of data infrastructure to support scientific analysis for the International GNSS Service[J]. Journal of Geodesy, 2009, 83(3): 309-325.
10. Dow J M, Neilan R E, Rizos C. The international GNSS service in a changing landscape of global navigation satellite systems[J]. Journal of geodesy, 2009, 83(3): 191-198.
11. Li R, Li L, Shi X, et al. An improved innovation-based protection level evaluation method for precise point positioning based on Kalman filter[J]. Measurement, 2026, 269: 120719.

12. Zhu Y, Zheng K, Cui X, et al. Preliminary analysis of the quality and positioning performance of BDS-3 global interop-erable signal B1C&B2a[J]. Advances in space research, 2021, 67(8): 2483-2490.

13. Geng J, Teferle F N, Shi C, et al. Ambiguity resolution in precise point positioning with hourly data[J]. GPS solutions, 2009, 13(4): 263-270.

14. Ge M, Gendt G, Rothacher M, et al. Resolution of GPS carrier-phase ambiguities in precise point positioning (PPP) with daily observations[J]. Journal of geodesy, 2008, 82(7): 389-399.

15. Geng J, Wen Q, Zhang Q, et al. GNSS observable-specific phase biases for all-frequency PPP ambiguity resolution[J]. Journal of Geodesy, 2022, 96(2): 11.

16. Gong X, Liu L, Guo R, et al. Improving real-time precise point positioning ambiguity resolution by considering uncali-brated phase delay uncertainty[J]. Measurement, 2025: 119165.

17. Shen Y, Li W, Xu G, et al. Spatiotemporal filtering of regional GNSS network's position time series with missing data using principle component analysis[J]. Journal of Geodesy, 2014, 88(1): 1-12.

18. Ji K, Shen Y, Wang F. Signal extraction from GNSS position time series using weighted wavelet analysis[J]. Remote Sensing, 2020, 12(6): 992.

19. Ren Y, Wang H, Lian L, et al. A method based on MTLS and ILSP for GNSS coordinate time series analysis with missing data[J]. Advances in Space Research, 2021, 68(9): 3546-3561.

20. Bouin M N, Vigny C. New constraints on Antarctic plate motion and deformation from GPS data[J]. Journal of Geo-physical Research: Solid Earth, 2000, 105(B12): 28279-28293.

21. Savchyn I, Brusak I, Tretyak K. Analysis of recent Antarctic plate kinematics based on GNSS data[J]. Geodesy and Geo-dynamics, 2023, 14(2): 99-110.

22. Kellevezir A, Tuşat E, Özlüdemir M T. Investigation of Plate Movements on the

Antarctic Continent and Its Surround-ings Using GNSS Data and Global Plate Models[J]. Geosciences, 2026, 16(3): 119.

23. Bahadur B, Nohutcu M. PPPH: a MATLAB-based software for multi-GNSS precise point positioning analysis[J]. GPS So-lutions, 2018, 22(4): 113.
24. Hatch R. The synergism of GPS code and carrier measurements[C]//International geodetic symposium on satellite dop-pler positioning. 1983, 2: 1213-1231.
25. Melbourne W G. The case for ranging in GPS based geodetic systems[C]//Proceedings 1st International Symposium on Precise Positioning with the Global Positioning System, US Department of Commerce, Rockville, Maryland, 1985.
26. Wübbena G. Software developments for geodetic positioning with GPS using TI 4100 code and carrier measure-ments[C]//Proceedings 1 st International Symposium on Precise Positioning with the Global Positioning System, US Dept. of Commerce, Rockville, Maryland, 1985.
27. Teunnissen P J G. The least-square ambiguity decorrelation adjustment: A method for fast GPS integer ambiguity esti-mation[J]. Journal of Geodesy, 1995, 70(1): 65-82.
28. Park J K, Kim M G, Lee J S. Tectonic motion monitoring of Antarctica using GPS measurements[J]. International Journal of Control and Automation, 2013, 6(2): 215-224.
29. Luzum B, Petit G. The IERS Conventions (2010): Reference systems and new models[J]. Proceedings of the International Astronomical Union, 2012, 10(H16): 227-228.
30. Hui T, Pengfei C, Jingzhong B I. Effect analysis of different interpolation methods on height time series of CORS[J]. Sci-ence of Surveying and Mapping, 2013, 38(1): 16-17.
31. Altamimi Z, Metivier L, Rebischung P, et al. ITRF2020 plate motion model[J].

Geophysical Research Letters, 2023, 50(24): e2023GL106373.